Applied Physics A (2020) 126:780
https://doi.org/10.1007/s00339-020-03893-9

Applied Physics A
Materials Science & Processing

Temperature dependent electrical properties of YSZ synthesized through microwave combustion

E. Satheeshkumar[1] · P. Prabunathan[2] · P. Anbarasi[1] · K. Ilango[1] · P. Manohar[1]

Received: 21 April 2020 / Accepted: 6 August 2020

Abstract
In the present work, Yttria Stabilized Zirconia (YSZ) was synthesized rapidly through microwave combustion. Subsequently, the synthesized YSZ was conventional sintered at different temperatures, ranging from 1200 to 1400 ºC at 50 °C intervals. X-ray diffraction results confirmed that the synthesized YSZ belongs to the cubic phase. Further, the investigation of microstructures of sintered YSZ using SEM analysis confirmed the temperature dependent grain growth behavior. Among the sintered YSZ, the sample sintered at 1400 ºC was found to possess the highest median particle size (4.77 µm), as well as average grain size (4.15 µm) with increased relative density (92%). Impedance studies for the YSZ samples sintered at different temperatures revealed that the conductivity is directly proportional to the relative density and operating temperature. Accordingly, the sample sintered at 1400 °C showed the highest ionic conductivity of 5.68×10^{-2} S/cm at 700 °C. The data resulted from various studies, suggesting that the YSZ synthesized through microwave assisted approach yields conductivity and dielectric behavior similar to conventional methods. Hence, this approach could also be extended to the synthesis of various electrolyte materials (E.g., LSDF, LSCO, and BSCF) that can be used in solid oxide fuel cells at a low cost and in a short duration.

Keywords YSZ · Sintering · Microwave combustion · Conductivity · Density

1 Introduction

Yttria Stabilized Zirconia (YSZ) has been extensively explored as an electrolyte in Solid Oxide Fuel Cells (SOFC) because of its high temperatures chemical stability [1–5]. In particular, 8 to 12% Yttria (Y_2O_3) Stabilized Zirconia (YSZ) delivers improved conductivity at elevated temperatures [6, 7]. Hence, different synthetic approaches such as sol–gel [8], co-precipitation [9], solid-state synthesis [10, 11], mechanical mixing of oxide powders (ball milling) [12], spray drying [13], hydrothermal synthesis [14], solution combustion synthesis [15] and conventional gel-combustion [16] have been adopted by various research groups to facilitate the synthesis of YSZ. In spite of individual merits, most of the methods have common limitations such as long duration, consumption of hazardous solvents, poor yield, etc. Almost, the solution based processes require conventional heating, which results in a non-consistent reaction throughout the bulk due to the rise of high thermal gradient effect. Great efforts are being made to prepare materials related to energy devices with an easy and facile approach without compromising the inherent properties [17–20].

Recently, microwave-assisted synthesis has been receiving great attention due to its various benefits such as (i) less time consumption, (ii) environmental friendly, (iii) low energy, and (iv) high yield of products [21]. The microwave assisted heating generates an "inverse heating effect", i.e., temperature is noticed to be higher in the reaction center compared to the surrounding, which finally lead to thermal runaway [22]. Microwaves will directly activate the molecules in the reaction mixture as opposite to other methods like oil bath, heating chamber, which transfers energy indirectly [23]. Here, the microwaves interact directly

Electronic supplementary material The online version of this article (https://doi.org/10.1007/s00339-020-03893-9) contains supplementary material, which is available to authorized users.

✉ P. Manohar
pmano55@yahoo.co.in

[1] Department of Ceramic Technology, A.C. Tech Campus, Anna University, Chennai 600025, India

[2] Polymer Engineering Laboratory, PSG Institute of Technology and Applied Research, Coimbatore 641032, India

Published online: 12 September 2020

with molecules and create heating, while the conventional approach generally spends much energy to cross the external boundaries. Comparing to environmental synthesis (e.g., oil-bath) the microwaves assisted approach saves energy about 85 fold times at laboratory scale [24]. These advantages of microwaves offers rapid one pot synthesis for wide variety of materials [25]. In this view, Vijay et al. 2014 studied microwave assisted gel-combustion synthesis of 8 mol % YSZ with three different fuels in addition to conductivity study. It was observed that the particles prepared were smaller in size with high density and good conductivity than that of the sample obtained by other combustion methods [26]. Nevertheless, the temperature dependent electrical properties of YSZ, prepared through rapid microwave synthesis, still remains unexplored. The dielectric properties of YSZ usually depend on various factors such as grain size, grain boundary, density and temperature.

Earlier, our group explored the synthesis of NiO/YSZ composites through microwave-assisted combustion and ascertained its suitability as anode material for SOFC by evaluating the electrical properties [27]. With this interest, the present work is intended to explore the temperature dependent electrical properties of YSZ prepared using microwave-assisted combustion, which builds the scope of the present study. A detailed study on crystallinity, microstructure, density, and conductivity of microwave assisted synthesized YSZ with respect to various temperatures were studied and reported in this paper.

2 Materials and methods

2.1 Materials

$ZrO(NO_3)_2.xH_2O$ (99.99%, Sigma-Aldrich, India), $Y(NO_3)_3.6H_2O$ (99.99%, CDH, New Delhi), and glycine from Alfa-Aesar were purchased and used as it is. The completer preparation of reaction mixture were carried out using double de-ionized (DI) water. ONIDA, Power Barbecue 28, 900 W, 2.4 GHz microwave oven was used to synthesis YSZ powders.

2.2 Synthesis of YSZ via microwave combustion

The stoichiometric amount of metal nitrates were dissolved in DI water along with 0.6 equivalent moles of glycine and stirred for 30 min in magnetic stirrer to get a homogeneous solution of metal ions. Further, the solution was heated at 80 °C and then cooled to form a gel. The synthesized gel was subjected to combustion in a microwave oven (900 W, 2.45 GHz frequency) for 15 min. The resulting sponge-like material was well grinded to yield a fine powder (YSZ). The obtained YSZ powder was further calcined at 800 °C for 2 h and then after cooling, it was grinded well to make the powder-free from agglomerates. The pellets were prepared out of the synthesized powders, with a uniaxial press. A pressure of 500 bar was applied to 0.5 g of powder to maintain a uniform density with 12 mm diameter and 1 mm thickness. The pellets as well as powders were then sintered for 4 h at different temperatures ranging from 1200 to 1400 °C at 50 °C intervals in a conventional electrical resistance furnace. The samples were labeled as YZ_1, YZ_2, YZ_3, YZ_4, and YZ_5 corresponding to their sintering temperatures of 1200, 1250, 1300, 1350, and 1400 °C respectively.

2.3 Characterization

The particle size of the prepared samples was analyzed using the Laser particle size analyzer (HORIBA LA-950, Japan). The required amount of powder sample was dispersed in ultrapure distilled water and subsequently, 0.02% of dispersant (sodium hexametaphosphate) was added to it and sonicated for 10 min before subjecting to analysis.

To determine the combustion temperature of the synthesized powders, the prepared gel was subjected to Differential Scanning Calorimeter (DSC) analysis using NETZSCH DSC-200PC (TA instruments USA) at a heating rate of 10 °C/min, from RT to 500 °C.

The as prepared YSZ, calcined, and sintered powder samples were subjected to XRD analysis (XRD 3003 TT, GE Inspection Technologies, Germany) using Cu K_α radiation. The diffraction data were obtained from $2\theta = 20$ to 85° with a step size of 0.02° (2θ).

For microstructural analysis, sintered pellets were sputtered with gold and an SEM (Hitachi S-3400 N, Japan) equipped with EDX (Horiba) was used to record the morphology along with the elemental composition at 20 kV. Then the average grain size was calculated from ImageJ software.

The sintered dimensions of the pellets were measured with the help of a digital Vernier caliper and the relative density of the pellets was measured using the Archimedes principle. The pellets were coated on both sides with silver paste and cured at 400 °C prior to electrical measurements. The electrical measurements were carried out in air using an Impedance analyzer (NumetriQ, PSM-1735, UK) in the temperature range of 50 to 700 °C at 50 °C intervals from 1 Hz to 1 MHz.

3 Results and discussion

3.1 Differential scanning calorimetry (DSC)

The combustion reaction of gel containing metal nitrates and glycine was studied using DSC analysis. Figure 1 presents

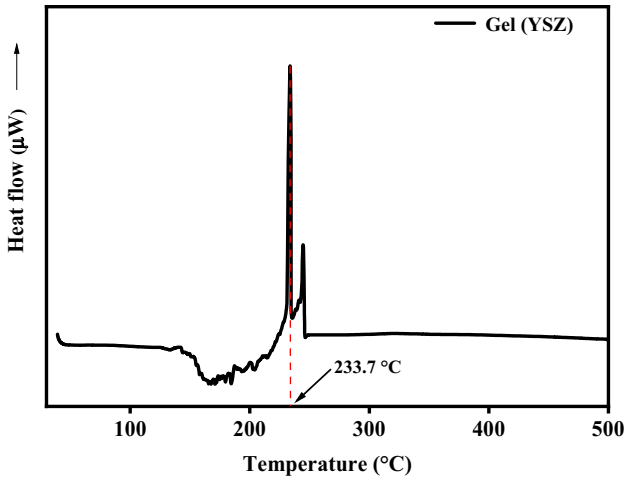

Fig. 1 DSC thermogram of precursor gel

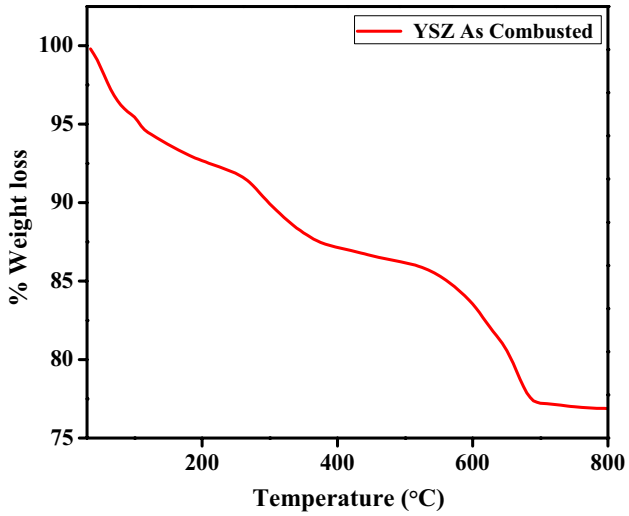

Fig. 2 TGA profile of the as combusted YSZ

the thermogram of YSZ gel subjected to DSC analysis performed from 30 °C to 500 °C. The exothermic peaks observed at 233.7 °C and 244.6 °C corresponds to the heat evolution during the combustion of the prepared gel. YSZ powders can be synthesized using different fuels like glycine, urea, etc. However, particles prepared using glycine show comparatively smaller crystallite size and higher specific surface area and densification than the particles obtained using other fuels [28]. The initial exothermic peak at 233.7 °C is attributed to the early decomposition of the nitrate precursors, whereas the successive exothermic peak at 244.6 °C corresponds to the decomposition of residual metal nitrates and carbon present in the gel [27, 29].

3.2 Thermo-gravimetric analysis

Thermo-gravimetric analysis was performed for the combusted YSZ in order to validate the degree of crystallization. Figure 2 depicts the thermogram of the combusted YSZ, which shows weight losses at three different stages between 30 and 800 ºC. The first stage of degradation which occurs below 250 °C accounts for 8% weight loss. This phenomenon is attributed to the removal of physically adsorbed water and chemically adsorbed hydroxyl groups. The second stage of weight loss which occurs from 251 to 500 °C is associated with the oxidation of organic compounds present in the powder due to the addition of glycine fuel. Final stage of decomposition was observed from 500 °C to 650 °C, which corresponds to the removal of nitrates residues [27, 30]. Beyond 650 °C, TGA pattern shows minor weight loss which is attributed to the crystallization of YSZ [31]. Beyond 800 °C, there occurs no change in thermogram, which confirms that the combusted YSZ was completely crystallized. Hence, the combusted YSZ was further calcined at 800 °C in order to facilitate the formation of complete crystalline phases of YSZ.

3.3 Diffraction analysis

The combusted, calcined and sintered YSZ samples were subjected to X-ray diffraction analysis in order to analyze its crystalline nature. The observed diffraction patterns of combusted and calcined YSZ are depicted in Fig. 3a along with sintered samples ($YZ_{1\text{-}5}$). The diffraction peaks appearing at 30.2°, 35.1°, 50.4°, 59.7°, 62.7°, 73.8°, 81.9° and 84.3° corresponds to (111), (200), (220), (311), (222), (400), (331) and (420) respectively. It is important to note that the phases formed were similar to that of conventionally prepared YSZ and it matches well with JCPDS card No. 301468 (YSZ). The diffractogram clearly demonstrates that no secondary phases were formed during the microwave-assisted synthesis. In addition, the d spacing value corresponding to the (111) plane of the combusted YSZ was observed to be 2.93 Å. Subsequently, the crystallite size was calculated using Debye Scherrer equation

$$D = \frac{0.9\lambda}{\beta \mathrm{Cos}\theta} \quad (1)$$

where, D is crystallite size, λ is the X-ray radiation wavelength, 2θ represents the diffraction angle and β is the full width half maxima of the major Bragg's peak. The crystallite size was observed to be 25 nm, which suggests that the YSZ prepared through microwave combustion results in nanometer size particles. Further, the XRD pattern of the calcined sample also delivers a similar diffraction peaks. However, the Braggs diffraction peaks become sharper and intense after calcination, in which the samples were subjected to

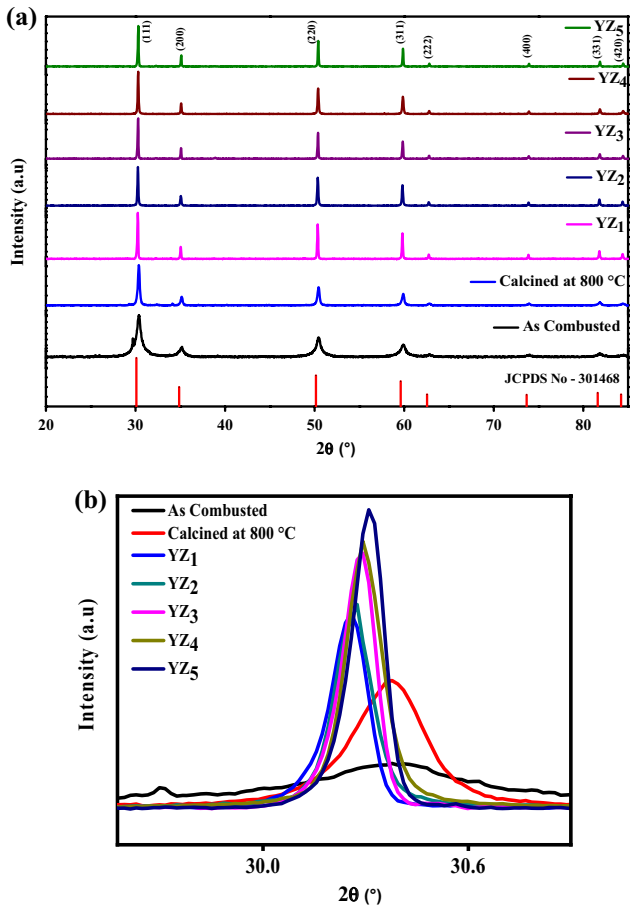

Fig. 3 **a** X-Ray Diffraction pattern of as combusted, calcined and sintered YSZ. **b** Diffraction plane (111) of as combusted, calcined and sintered YSZ

high temperature. During calcination, the YSZ particles tend to attain its crystalline structure through the removal of chemically adsorbed water, unreacted nitrates and organic matter from the YSZ phases. This behavior is in accordance with the result observed in TGA analysis, which was shown in Fig. 2.

The density of YSZ plays a major role in tailoring the electrical properties. Thus, it is highly desirable to densify the calcined YSZ. Accordingly, the calcined YSZ was further subjected to sintering at different temperatures starting from 1200 to 1400 °C. The samples sintered ($YZ_{1\text{-}5}$) at different temperatures were also show similar Braggs diffractions and confirming the existence of cubic crystal structures (Fig. 3a). It was observed that the crystallinity of YSZ increases with increase in sintering temperature. This behavior was well documented in Fig. 3b, using the (111) plane of Bragg's diffraction. The increase in sharpness and intensity of the peaks are due the formation of the polycrystalline phase of YSZ [32–34]. In spite of the variations in sintering temperatures, no significant change in d spacing was observed (Table 1). This infers that the samples $YZ_{1\text{-}5}$ possess almost similar d-spacing value with the retention of cubic crystalline structure.

3.4 Particle size and density analysis

Particle size analysis was performed and the obtained particle size distribution plots of combusted YSZ and sintered $YZ_{1\text{-}5}$ were presented in Fig. 3. The combusted YSZ shows narrow particle size distribution ranging from 0.6 to 1.3 µm (Fig. 3a), which is significant when compared to those of existing reports [35, 36]. The median particle size value (D_{50}) of the combusted YSZ is found to be 0.88 µm. Furthermore, a gradual increase in D_{50} value (Fig. 3b–f) confirms the growth of particles, as an effect of sintering which is given in Table 2. In addition, the relative densities of the sintered samples were also measured using Archimedes principle and tabulated in Table 2 in order to evaluate the effect of sintering.

$$\rho = \frac{W_D - \rho_w}{W_w - W_s} \tag{2}$$

where, ρ is Bulk density of the sample, W_D is Dry weight of the sample, ρ_w is density of water, W_w is wet weight of the sample, W_s is suspended weight of the sample. The calculated relative density values were tabulated in Table 2. The

Table 1 d-spacing and crystallite sizes of as combusted, calcined and sintered YSZ

Sample	d- spacing (Å)		
	(111) plane	(220) plane	(311) plane
As combusted	2.9310	1.7901	1.5387
Calcined at 800 °C	2.9397	1.8073	1.5387
YZ_1	2.9541	1.8113	1.5479
YZ_2	2.9518	1.8109	1.5458
YZ_3	2.9505	1.8106	1.5449
YZ_4	2.9498	1.8085	1.5432
YZ_5	2.9473	1.8053	1.5417

Table 2 Density, relative density and average grain size of $YZ_{1\text{-}5}$

Sample	Median particle size (D_{50}) (µm)	Relative density (%)	Average grain size (µm) (From SEM)
YZ_1	2.76	81	3.16 (±0.21)
YZ_2	3.50	82	3.28 (±0.35)
YZ_3	3.64	83	3.42 (±0.71)
YZ_4	3.91	91	3.88 (±0.57)
YZ_5	4.77	92	4.15 (±0.48)

relative density value of the YZ_5 sample sintered at 1400 °C is 92%, whose value is nearly 11% higher than sample sintered at 1200 °C (YZ_1, whose relative density value is 81%). This phenomenon is due to the formation of close packed cubic structure of YSZ at elevated sintering temperature. Table S1 (supporting information) details about the theoretical density (%)grain size (μm) and conductivity (S/cm) of YSZ samples prepared using different methods. It is noteworthy that the relative density of the YSZ prepared using microwave assisted synthesis is observed to slightly higher than those of YSZ prepared using solution combustion and commercial purchased (Table S1). This result suggest that the microwave assisted synthesis could be an effective alternate to conventional combustion route [37]. However, the relative density of the present case is comparatively lower than other approaches (hydrothermal and sol–gel) [38, 39]. This can be studied in detail through optimizing the precursor as well as gel concentration, solvent effect in future studies.

3.5 Morphological studies

Microstructure analysis was performed for $YZ_{1\text{-}5}$ sintered samples to evaluate grain structures along with their packing nature. The observed micrographs were presented in Fig. 4a–e. In Fig. 4a, the appearance of discrete grains along with voids at the interfaces confirms the low density nature of YZ_1. The size of the grains become more proportionate with increase in sintering temperature, which in turn reduces the voids present in between the individual grains

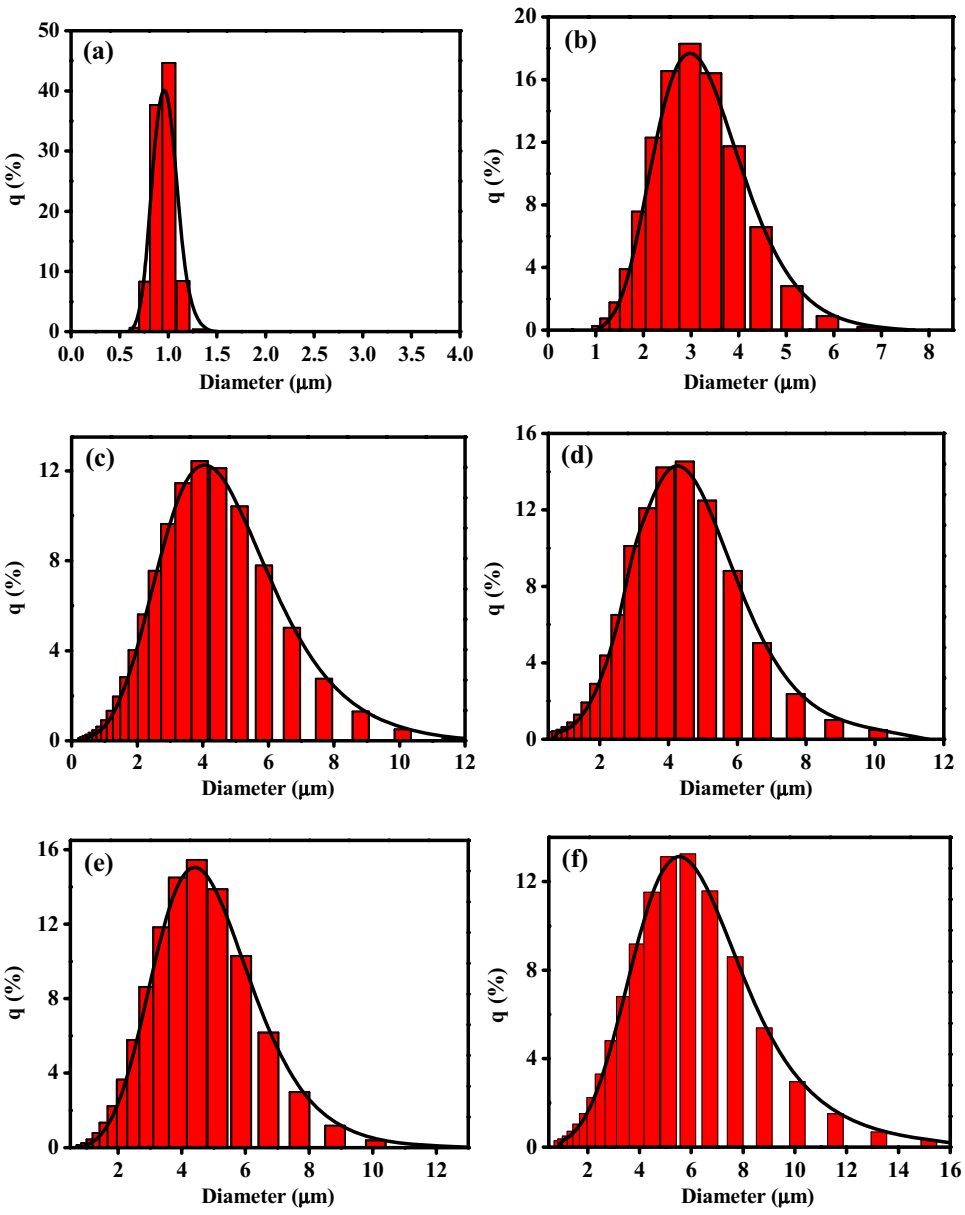

Fig. 4 Particle size distribution curve of **a** as combust YSZ and **b–f** samples of $YZ_{1\text{-}5}$

(Fig. 4b–d). The increase in the degree of crystallization due to the enhanced interfacial interaction between individual grains contributes to the grain growth [40]. This phenomenon could be evidenced while comparing the micrograph of YZ_1 with YZ_5 which were sintered at 1200 and 1400 °C respectively. The grain growth due to crystallization and densification delivers less voids and very close grain structure (Fig. 4e). This growth phenomenon occurs as the function of temperature, which in turn increases the average grain size (Table 2). The $YZ_{1\text{-}5}$ samples show an average grain sizes of 3.16, 3.28, 3.42, 3.88 and 4.15 µm respectively (Fig. 4a–e). The grain size of YSZ was found to be increasing with an increase in sintering temperature. These results are in good agreement with the densities calculated from the Archimedes principle. Due to the closure of voids at high temperature, the overall grain size of YSZ gets increased [41, 42]. Further, the elemental analysis on the YZ_5 sample was observed by EDX. The obtained results are presented in Fig. 4f. The binding energy peaks observed in Fig. 4f are assigned to the respective elements such as Y, Zr and O. From the intensity of the signals, the semi-quantitative amount of Y, Zr and O are found to be 2.89%, 12.63% and 84.49% respectively. In the present case, the Y/Zr ratio is observed higher than the earlier reports [43, 44]. This might be attributed to the overlapping of both Y and Zr peaks.

3.6 Electrical properties

3.6.1 Temperature dependent dielectric constant, dielectric loss, resistivity and conductivity

Electrical properties such as dielectric constant, dielectric loss, resistivity and conductivity of $YZ_{1\text{-}5}$ were studied using impedance analyzer at a range of temperatures from 50 to 700 °C. Figure 5a shows the dielectric constant behavior of $YZ_{1\text{-}5}$, in which a uniform stable trend was observed up to 500 °C, beyond which the dielectric constant values are increased. The frequency independent real part of relative permittivity is calculated using the formula

$$\varepsilon' = \frac{C_p t}{\int_0 A} \tag{3}$$

where, C_p – parallel capacitance (Farad), t – thickness of the pellet, ε_0 – absolute permittivity of free space (8.854×10^{-12} F/m), A – cross sectional area of the pellet, the dielectric constant values begin to increase, which attributes for the orientation of dipoles. At high temperatures, the orientations of dipoles are facilitated, which is due to the thermal activation of molecules [45, 46]. The random motion and un-aligned dipoles produced due to thermal activation of molecules subsequently increases the values of dielectric constant at higher frequency and at elevated temperatures. The dielectric loss behavior of the samples was shown in Figure S1. In general, electrical flux density of the materials will not follow the phase of the applied electric field. Hence, there will be some phase lag between the electrical flux and applied electric field contributed by the inertia of the materials dipoles, which in turn leads to the loss (dielectric loss) in the material in form of heat. In the present case, no significant dielectric loss was noticed up to 500 °C against the applied frequency 1 MHz. However, the change in polarization of molecules after 500 °C, contributes to the occurrence of significant dielectric losses in the material. This increased value of dielectric loss is due to the thermal activation of dipoles, where charge carriers begin to orient and contribute to the conduction mechanism [47]. Figure 5b shows the decrease in resistivity of YSZ due to transition from insulation to metallic character, which becomes drastically higher beyond 500 °C. This is due to the formation of a conductivity path through the formation of vacancies and thermal activation of oxygen ion migration at elevated temperature [48–51].

3.6.2 Frequency-dependent behavior of dielectric constant, dielectric loss and resistivity

The frequency dependent nature of $YZ_{1\text{-}5}$ at 700 °C were carried out. The observed frequency-dependent behavior of dielectric constant and resistivity of $YZ_{1\text{-}5}$ from 1 Hz to 1 MHz were presented in Fig. 6a–b and the values are tabulated in Table 3. The dielectric constant values of $YZ_{1\text{-}5}$ decrease, as the frequency increases (Fig. 6a), which is due to the change in polarization of dipoles particularly at high frequency. The polarization mechanism includes the orientation of various types of polarizations such as space charge orientation, ionic and electronic polarization. At high frequency, such polarizations are not well aligned, which in turn, decreases the dielectric constant [52, 53]. At 1 MHz, the dielectric constant values of YZ_1, YZ_2, YZ_3, YZ_4 and YZ_5 are 130, 152, 238, 276 and 280 respectively. The sample sintered at 1400 °C (YZ_5), tends to show the highest dielectric constant than those of other samples. This phenomenon is attributed due to the formation of larger grains structures and density for the samples sintered at 1400 °C as evident from SEM.

The dielectric loss behavior of $YZ_{1\text{-}5}$ at 700 °C shown in Figure S2, also delivers a trend similar to dielectric constant. At low frequencies (10–10^2 Hz), the dipoles of $YZ_{1\text{-}5}$ utilize the available energy for their orientation as well as for their polarization, which in turn causes a low dielectric loss. However, at moderate frequencies ranging from 10^2 to 10^5 Hz, the migration and polarization of ions, followed by the conduction loss occurs due to the availability of sufficient energy. This phenomenon contributes to the

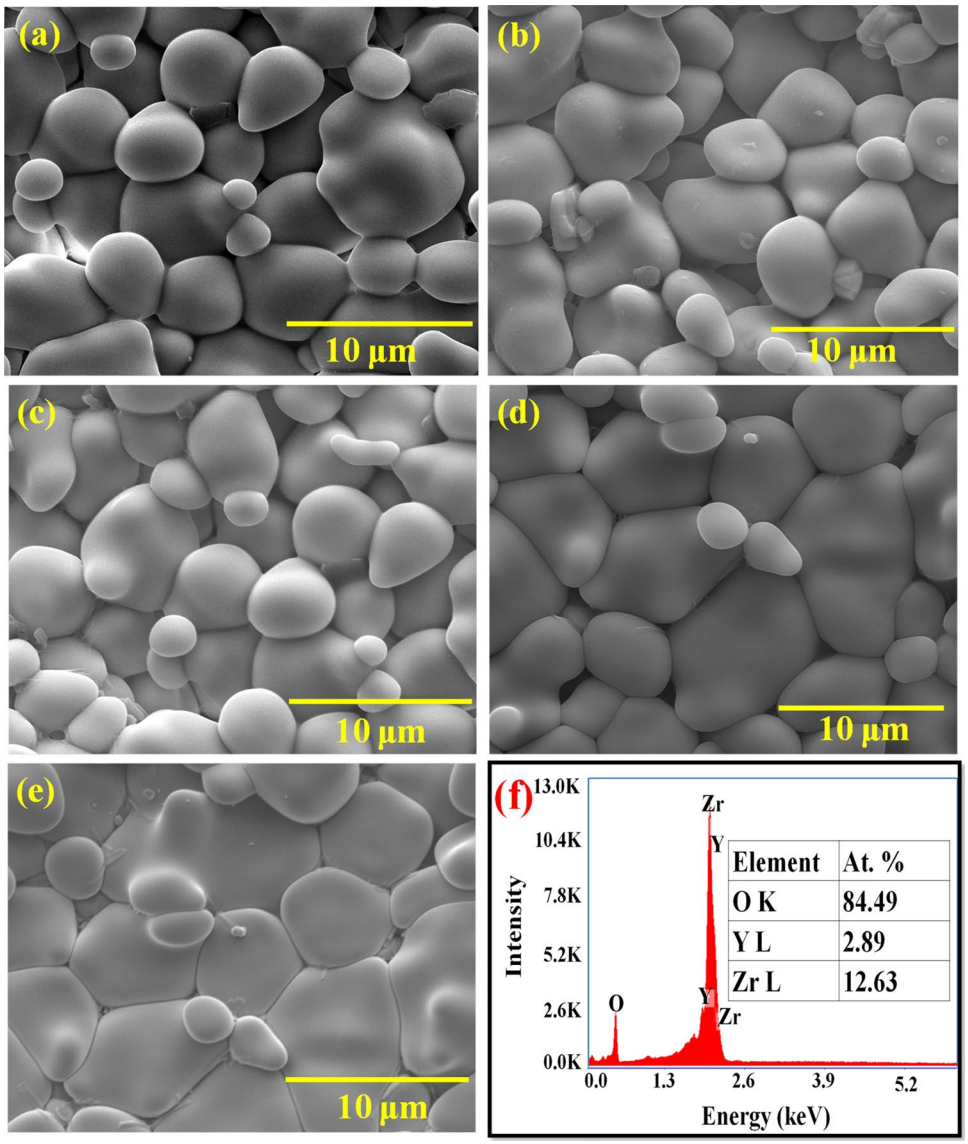

Fig. 5 **a**–e SEM micrographs of sintered $YZ_{1\text{-}5}$ samples and **f** EDX profile of YZ_5

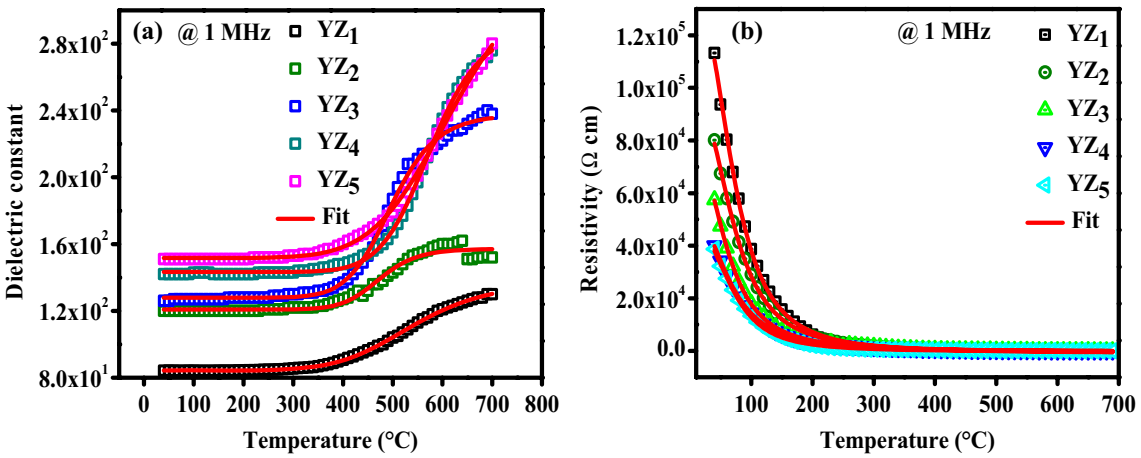

Fig. 6 Temperature dependent **a** dielectric constant, and **b** resistivity of $YZ_{1\text{-}5}$ from 50 to 700 °C at 1 MHz

Table 3 Electrical properties of YZ_{1-5} at 1 MHz and 700 °C

Sample	Electrical properties @ 700 °C @ 1 MHz			
	dielectric constant	Dielectric loss	Resistivity (Ωcm)	Conductivity $(Scm^{-1})\times10^{-2}$
YZ_1	130	3.51	70	1.42
YZ_2	152	3.76	52	1.91
YZ_3	238	4.01	44	2.26
YZ_4	276	4.02	22	4.47
YZ_5	280	5.98	19	5.17

dielectric loss behavior of YZ_{1-5}. Furthermore, the dielectric loss values at higher frequency starts to decrease due to the restricted orientation and polarization of charged species, which contributes to the lower dielectric loss in the material [54, 55]. Similar to dielectric constant, the dielectric loss values are also observed to increase as the sintering temperature increases. At 1 MHz, the dielectric loss values of YZ_1, YZ_2, YZ_3, YZ_4 and YZ_5 are 3.51, 3.76, 4.01, 4.02, and 5.98 respectively. The highest dielectric loss is associated with samples sintered at 1400 °C. This is associated due to the formation of more charge-transfer behavior, which also contributed for higher dielectric constant value.

The frequency-dependent resistivity of YZ_{1-5} samples at 700 °C is shown in Fig. 6b. The resistivity of YZ_{1-5} gradually decreases with increasing frequency. This infers that the mobility of ions increases as the frequency shifts from 1 Hz to 1 MHz, which results in a gradual drop in the resistivity behavior. Among the resistivity of YSZ sintered at different temperatures, the sample YZ_5 sintered at 1400 °C, shows the least resistance of 19 Ωcm at 1 MHz, (Table 3). As a consequence of formation of a conductive path, the charge-transfer behavior process is favored either inter or intra grains of YSZ. Thus, it is important to note the conductivity value of the sample YZ_5, which is also found to 5.17×10^{-2} S/cm. As the grain size of YZ_5 is higher than those of other samples YZ_{1-4}, the resistance could be significantly contributed only from grain boundary and leading to higher conductivity. The conductivity value obtained is nearly equivalent to those reported by various authors in the literature [56, 57]. Similarly, a conductivity of 1.85×10^{-4} S/cm is obtained at 560 °C for the sample sintered at 1500 °C [58]. Also, a conductivity value of 3×10^{-2} S/cm was achieved at 800 °C for sol–gel synthesized YSZ sintered at 1400 °C [57]. From these results, it can be observed that the microwave assisted synthesized samples also deliver equivalent temperature dependent electrical properties as those of samples prepared by conventional combustion method and other time consuming hydrothermal approaches [14].

3.6.3 Conductivity behavior

The activation energy of YZ_{1-5} was calculated from Arrhenius equation

$$\sigma = \frac{A}{T}\exp\left(-\frac{E_a}{KT}\right) \tag{4}$$

To obtain activation energy (E_a) in terms of eV

$$E_a = \text{Slope}\times 8.61\times10^{-2}eV \tag{5}$$

Figure 7 presents the Arrhenius plots and the activation energy values were tabulated in Table 3. Compared to high temperature, the activation energy (E_a) is noticed to be greater at low temperature. The activation energy observed for the YZ_{1-5} at high temperature is almost equal to that of bulk YSZ. Further, the Arrhenius plot presented in Fig. 7 shows a non-linearity at high temperature. This phenomenon could be attributed to the change in conductivity behavior.

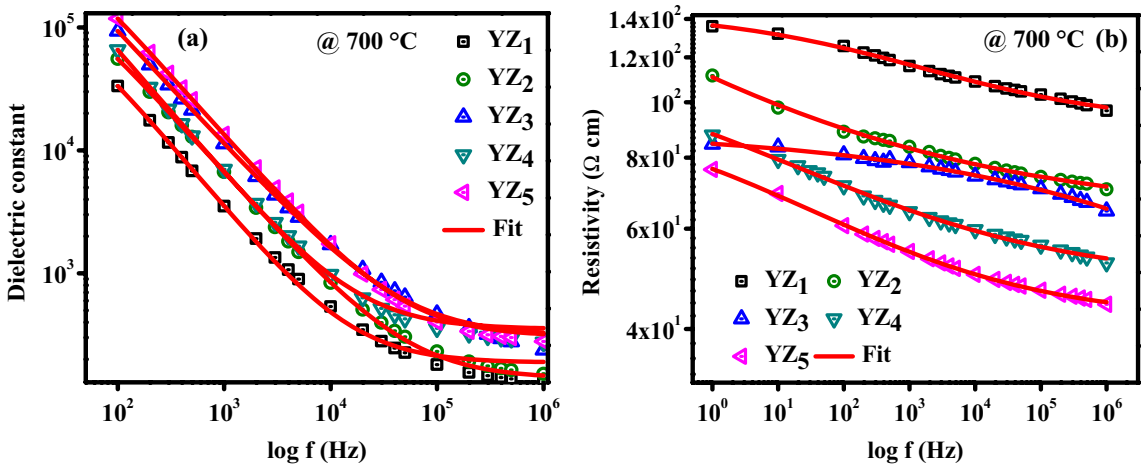

Fig. 7 Frequency dependent **a** dielectric constant, and **b** resistivity of YZ_{1-5} samples at 700 °C

The change is attributed to the shifting of ionic conductivity from intergrain to intragrain behavior during high temperatures exposure [59]. In general, there are two models to interpret the non-linearity in Arrhenius plot of zirconia-based electrolyte, which referred to intragrain–intergrain conductivity model and dissociation–migration energy model [60]. To the observed total conductivity, the intergrain model contributes less to the total conductivity than the intragrain conductivity at high temperature. On the other hand, at low temperature, the intergrain conductivity plays a key role on the ionic conductivity. Few other reports also suggest that the conductivity nature of zirconia based electrolyte can be significantly improved at lower temperatures by increasing the grain size [61].

To detail the conducting mechanism, the slope of the plot of log ω vs log σ_{ac} (Fig. 8) was calculated. The frequency dependant conductivity has the form,

$$\sigma_{ac}(\omega) = A\omega^{s} \tag{6}$$

where ω is angular frequency and exponent s is less than or equal to unity. The temperature-dependent behavior of the frequency exponent gives detailed information about the suitable mechanism involved in AC conductivity. The '*s*' parameter for $YZ_{1\text{-}5}$ presented in Fig. 8 showed a similar trend with an increase in temperature. This is supported by the Correlated Barrier Hopping (CBH) model. According to CBH, bipolarons hop over a barrier separating the charged defects instead of tunneling through it. This leads to an enhanced conductivity at higher temperatures [28, 62–64].

In addition to support the electrical behavior, electrochemical impedance spectroscopy (EIS) was performed to determine the conductivity behavior. As shown in Fig. 9, the

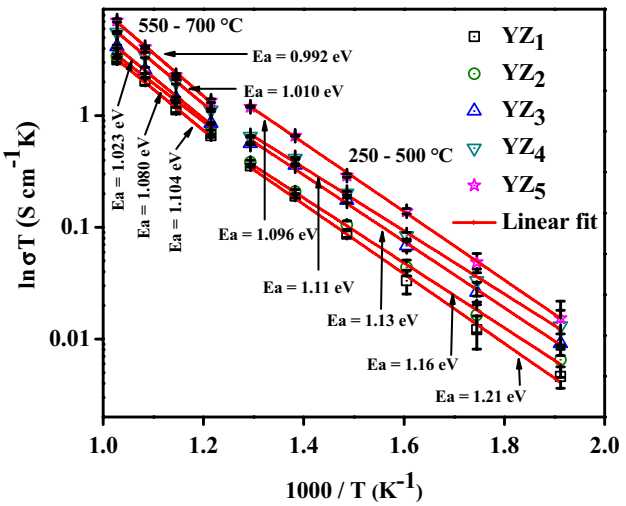

Fig. 8 Arrhenius plot of $YZ_{1\text{-}5}$ samples

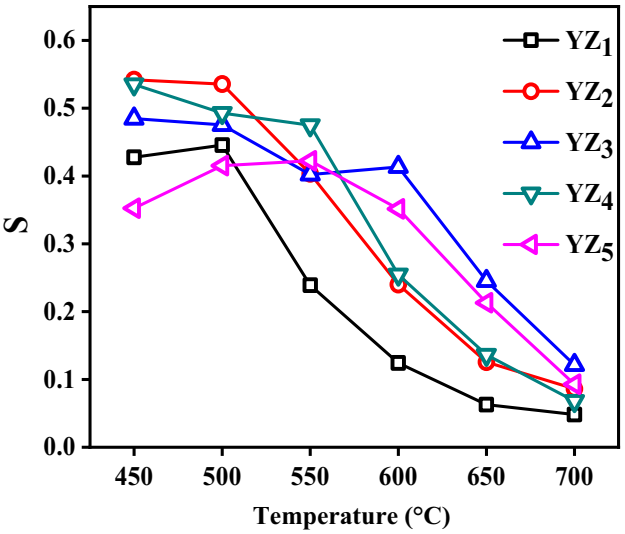

Fig. 9 'S' Parameter (frequency Exponent) with respect to temperature for the samples $YZ_{1\text{-}5}$

complex Nyquist plots of the $YZ_{1\text{-}5}$ measured at 400–700 °C temperatures in a frequency range between 1 Hz and 1 MHz delivers broad semicircles. The observed impedance curve are fitted with equivalent circuit shown in Figure S3 (supporting information). The broadness of the semicircles is observed to be restricted as the sintering temperature increases. Further, it was also noticed that the radius of the semicircles decreases with increasing in operating temperature Thus, it can be clearly understood that the conductivity of the grain boundary changes significantly due to formation of charge-transfer aided by temperature [38, 65]. In particular, the AC conductivity increases with increase in temperature Fig 10. As a consequence of high temperature, there arises point defect in YSZ electrolytes, which can favor ionic transport behavior.

4 Conclusion

In the present work, microwave-assisted combustion synthesis of YSZ was demonstrated in short duration using glycine as fuel. YSZ prepared through microwave-assisted combustion also possesses cubic crystalline phase similar to those of sample prepared using other synthesis methods like sol–gel, hydrothermal, combustion. Further, the effect of sintering temperature of YSZ influences the crystal growth as well as density, which were confirmed from the diffractogram and microstructure resulted from XRD and SEM analysis. Also, the reduction of grain boundary regions in the sintered YSZ contributes to the improvement in the electrical properties of the material such as conductivity. Thus, the rapid microwave-assisted combustion synthesis approach can be

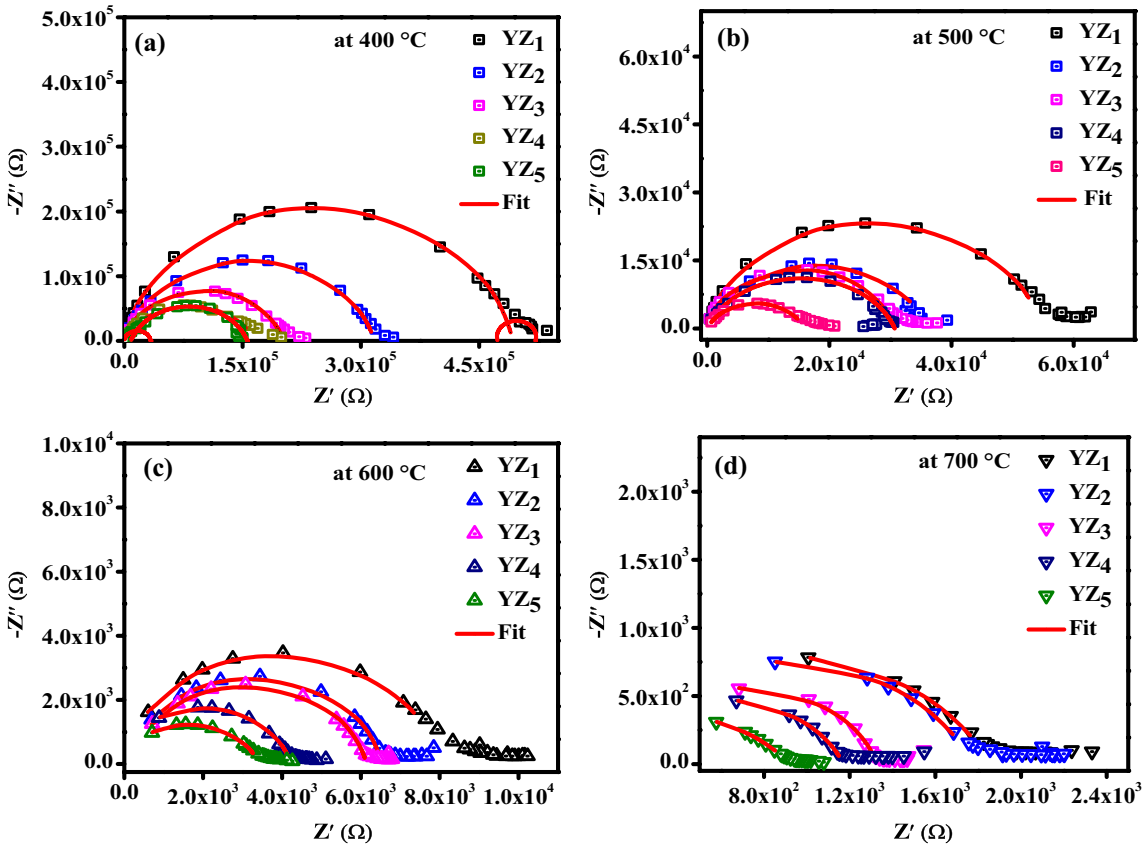

Fig. 10 Impedance spectroscopy at different temperature of the $YZ_{1\text{-}5}$

adopted for the synthesis of similar types of SOFC electrolytes (E.g., LSDF, LSCO, and BSCF, Ce, Sc and Y doped zirconia) in short duration.

References

1. Y. Mizutani, K. Hisada, K. Ukai, H. Sumi, M. Yokoyama, Y. Nakamura, O. Yamamoto, J. Alloys. Compd. **408**, 518 (2006)
2. N.P. Brandon, S. Skinner, B.C. Steele, Annu. Rev. Mater. Res. **33**, 183 (2003)
3. D.J. Brett, A. Atkinson, N.P. Brandon, S.J. Skinner, Chem. Soc. Rev. **37**, 1568 (2008)
4. J.B. Young, Annu. Rev. Fluid. Mech. **39**, 193 (2007)
5. J.A. Kilner, M. Burriel, Annu. Rev. Mater. Res. **44**, 365 (2014)
6. T.H. Etsell, S.N. Flengas, Chem. Rev **70**, 339 (1970)
7. S.P.S. Badwal, Solid State Ionics **52**, 23 (1992)
8. O.M. Hajizadeh, R.S. Razavi, M. Khajelakzay, J. Sol-Gel, Sci. Technol **73**, 227 (2015)
9. D.H. Prasad, H.R. Kim, J.S. Park, J.W. Son, B.K. Kim, H.W. Lee, J.H. Lee, J. Alloys. Compd. **495**, 238 (2010)
10. A. Suda, T. Kandori, Y. Ukyo, H. Sobukawa, M. Sugiura, J. Ceram. Soc. Jpn. **108**, 473 (2000)
11. K. Nomura, Y. Mizutani, M. Kawai, Y. Nakamura, O. Yamamoto, Solid State Ionics **132**, 235 (2000)
12. S. Indris, D. Bork, P. Heitjans, J. Mater. Synth. Process. **8**, 245 (2000)
13. Z. Wang, R. Hui, N. Bogdanovic. Z. Tang, S. Yick, Y. Xie, I. Yaroslavski, A. Burgess, R. Maric, D.J. Ghosh, Power Sources. **170**, 145 (2007)
14. F. Li, Y. Li, Z. Song. F. Ma, K. Xu, H.J. Cui, Eur. Ceram. Soc. **35**, 2361 (2015)
15. A. Varma, A.S. Mukasyan, A.S. Rogachev, K.V. Manukyan, Chem. Rev. **116**, 14493 (2016)
16. M. Marinšek, K. Zupan, J. Maeek, J. Power Sources. **106**, 178 (2002)
17. P. Prabunathan, A. Hariharan, M. Alagar, Polymer Plastics Technol. Eng. **55**, 542 (2016)
18. Y.Y. Kannangara, P. Prabunathan, J.K. Song, New. J. Chem **42**, 15387 (2018)
19. P. Kumar, N.K. Singh, R.K. Singh, P. Singh, Appl. Phys. A **121**, 635 (2015)
20. J. Liu, S. Bai, Appl. Phys A **123**, 293 (2017)
21. M.J, Gronnow, R. J. White, J.H. Clark, D. J. Macquarrie, Org. Process Res. DeV. **9**, 516 (2005)
22. A. de la Hoz, A. Diaz-Ortiz, A. Moreno, Angew. Chem. Int. Ed. **121**, 8471 (2009)
23. K. Morsi, J. Mater Sci **47**, 68 (2012)
24. C.A. Bizzi, M.F. Pedrotti, J.S. Silva, J.S. Barin, J.A. Nóbrega, E.M.M. Flores, J. Anal. Atom. Spectrom **32**, 1448 (2017)
25. J.-S. Xu, Y.-J. Zhu, Cryst. Eng. Comm. **14**, 2630 (2012)
26. S.K. Vijay, V. Chandramouli, S. Khan, P.C. Clinsha, S. Anthonysamy, Ceram Int. **40**, 16689 (2014)
27. E. Satheeshkumar, P. Anbarasi, K. Ilango, P. Prabunathan, P. Manohar, Mater. Technol. **32**, 638 (2017)

28. C.A. Da Silva, N.F. Ribeiro, M.M. Souza, Ceram Int. **35**, 3441 (2009)
29. S.J. Rajoba, L.D. Jadhav, P.S. Patil, D.K. Tyagi, S. Varma, B.N. Wani, J. Electron. Mater. **46**, 1683 (2017)
30. R. Li, C. Zhang, J. Liu, J. Zhou, L. Xu, Appl. Phys. A **125**, 773 (2019)
31. T. He, Q. He, N. Wang, J. Alloys, Compd **396**, 309 (2005)
32. T. Talebi, M. Haji, B. Raissi, Int. J. Hydrogen Energy. **35**, 9420 (2010)
33. O.J. Durá, M.L. de la Torre, L. Vázquez, J. Chaboy, R. Boada, A. Rivera-Calzada, J. Santamaria, C. Leon, Physical. Rev. B. **81**, 184301 (2010)
34. K. Rajeswari, M.B. Suresh, U.S. Hareesh, Y.S. Rao, D. Das, R. Johnson, Ceram. Int. **37**, 3557 (2011)
35. P. Carpio, E. Bannier, M.D. Salvador, A. Borrell, R. Moreno, E. Sánchez, Surf. Coat. Technol. **268**, 293 (2015)
36. A.T. Duong, D.R. Mumm, J. Electrochem. Soc. **159**, B39 (2011)
37. Q. Wang, R. Peng, C. Xia, W. Zhu, H. Wang, Ceram. Int. **34**, 1773 (2008)
38. J. Zhang, X. Huang, H. Zhang, Q. Xue, H. Xu, L. Wang, Z. Feng, RSC Adv. **7**, 39153 (2017)
39. T. Liu, J. Fang, S. Li, C. Wang, C. Ji, J. Ceram. Soc. Jap. **123**, 554 (2015)
40. A. Infortuna, A.S. Harvey, L.J. Gauckler, Adv. Funct. Mater. **18**, 127 (2008)
41. H. Zhu, R.S. Averback, Mater. Manuf. Process. **11**, 905 (1996)
42. H. Zhao, X. Li, F. Ju, U. Pal, J. Mater. Process. Technol. **200**, 199 (2008)
43. H.J Ko, J.H. Myung, S.H. Hyun, J.S. Chung, J. Appl. Electrochem. **42**, 209 (2012)
44. K. Sarkar, S. Mukherjee, S. Mukherjee, M.K. Mitra, J. Inst. Eng. India Ser. D. **95**, 135 (2014)
45. C. Wang, N. Zhang, Q. Li, Y. Yu, J. Zhang, Y. Li, H. Wang, J. Am. Ceram. Soc. **98**, 148 (2015)
46. O.P. Nautiyal, S.C. Bhatt, Am. J. Condens. Matter. Phys. **1**, 8 (2011)
47. X. Huang, H. Zhang, Y. Lai, J. Li, Appl. Phys. A **123**, 317 (2017)
48. P. Jena, S. Jayasubramaniyan, P.K. Patro, R.K. Lenka, A. Sinha, P. Muralidharan, E.S. Srinadhu, N. Satyanarayana, Appl. Phys. A **124**, 125 (2018)
49. A. Sen, Appl. Phys. A **126**, 36 (2020)
50. M.D. Stamate, Appl. Surf. Sci. **218**, 318 (2003)
51. R.V. Mangalaraja, S. Ananthakumar, P. Manohar, F.D. Gnanam, M. Awano, Mater. Lett. **58**, 1593 (2004)
52. A. Kumar, S.S. Yadava, P. Gautam, A. Khare, K.D. Mandal, J. Electroceramics **42**, 47 (2019)
53. N.H. Perry, T.C. Yeh, T.O. Mason, J. Am. Ceram. Soc **94**, 508 (2011)
54. R. Kumar, M. Zulfequar, T.D. Senguttuvan, J. Electroceramics **42**, 41 (2019)
55. S.K. Patri, P.L. Deepti, R.N.P. Choudhary, B. Behera, J. Electroceramics **40**, 338 (2018)
56. T. He, Q. He, N. Wang, J. Alloys. Compd. **396**, 309 (2005)
57. E. Courtin, P. Boy, T. Piquero, J. Vulliet, N. Poirot, C. Laberty-Robert, J. Power Sources. **206**, 77 (2012)
58. C. Korte, A. Peters, J. Janek, D. Hesse, N. Zakharov, Phys. Chem. Chem. Phys **10**, 4623 (2008)
59. C. Zhang, C.J. Li, G. Zhang, X.J. Ning, C.X. Li, H. Liao, C. Coddet, Mater. Sci. Eng. B **137**, 24 (2007)
60. J.B. Bauerle, J. Phys. Chem. Solids. **30**, 2657 (1969)
61. M. Aoki, Y.M. Chiang, I. Kosacki, L.J. Lee, H.L. Tuller, Y. Liu, J. Am. Ceram. Soc. **79**, 1169 (1996)
62. A. Pugazhendhi, S. Ellappan, I. Kumaresan, M. Paramasivam, Appl. Phys. A. **123**, 407 (2017)
63. S. Subramanian, D.P. Padiyan, J. Mater. Sci. **44**, 6040 (2009)
64. A. Pugazhendhi, S. Ellappan, I. Kumaresan, M. Paramasivam, Ionics **24**, 3745 (2018)
65. H.C. Yao, X.W. Wang, H. Dong, R.R. Pei, J.S. Wang, Z.J. Li, Ceram. Int. **37**, 3153 (2011)